IEEE Access
Multidisciplinary ⋮ Rapid Review ⋮ Open Access Journal

Received 21 March 2024, accepted 30 March 2024, date of publication 3 April 2024, date of current version 22 April 2024.

Digital Object Identifier 10.1109/ACCESS.2024.3384485

RESEARCH ARTICLE

A Method for Damage Detecting of Large Reflector Antennas Wheel-Rail Based on Electromagnetic Ultrasonic Technology

CONG JIN[1], YOU BAN[1,2], AND SHUFEI FENG[3]

[1]School of Intelligent Manufacturing Modern Industry (School of Mechanical Engineering), Xinjiang University, Ürümqi 830047, China
[2]Xinjiang Astronomical Observatory, Chinese Academy of Sciences, Ürümqi 830011, China
[3]School of Mechanical Engineering, Dongguan University of Technology, Dongguan 523808, China

Corresponding author: You Ban (banyou_xd@163.com)

This work was supported in part by the National Natural Science Foundation of China (NSFC) under Grant 52165053 and Grant 12303094, in part by China Postdoctoral Science Foundation under Grant 2021M702751 and Grant 2023T160549, in part by the Natural Science Foundation of Xinjiang Uygur Autonomous Region under Grant 2022D01C683, in part by the Doctor Scientific Research Project of Xinjiang University under Grant 620320037, and in part by Guangdong Basic and Applied Basic Research Foundation under Grant 2020A1515111043 and Grant 2023A1515010703.

ABSTRACT The azimuth wheel-rail of large reflector antennas is one of the key components, it not only supports the whole weight of the antenna, but also directly affects the antennas' pointing performance by its surface accuracy. Usually, the whole weight of the large reflector antenna is thousands of tons, its azimuth frame rollers have great contact stress with the wheel-rail surface, repeated rolling can cause rolling contact fatigue on the wheel-rail surface, resulting in wear, cracks and other damage to the wheel-rail, and even lead to failure or fracture of the wheel-rail in serious cases, so it is very important to monitor the damage of the antenna wheel-rail. Current studies are based on Hertzian theory for stress analysis of rollers and wheel-rails, it cannot visually determine the damage. In order to visually detect the usage of antenna wheel-rail surfaces, this paper, for the first time, proposed the method using electromagnetic ultrasonic detection to detect the damage of antenna wheel-rail surface. Based on the principle of electromagnetic ultrasonic nondestructive testing, the simplified wheel-rail model containing wear, corrosion and crack damages are simulated. The results show that this method can effectively detect the surface damage of the antenna wheel-rail surface, and it can provide an important reference for the research of wheel-rail damage detection of large reflector antennas.

INDEX TERMS Large reflector antenna, azimuth wheel-rail, surface damage, electromagnetic ultrasonic detection.

I. INTRODUCTION

With the rapid development of deep space exploration and radio astronomy, the large reflector antenna plays an increasingly prominent role and has become an indispensable and important equipment in related research directions [1]. At present, the world's famous large reflector antennas are mainly constructed and used by big and powerful countries, China is also actively contributing to deep space exploration and radio astronomy research. For example, QTT (QiTai Radio Telescope), the world's largest fully movable high-performance radio telescope, is being built in Qitai, Xinjiang, China. With a diameter of 110 meters and a weight of about 6,000 tons, its operating frequency band is 150MHz-115GHz and it is expected to be completed in 2028 [2], [3], [4], [5].

The large reflector antenna is heavy and usually uses a large wheel-rail to support its orientation operation, the Green Bank Telescope (GBT) of 110 × 100 meters in Figure 1(a) is a typical wheel-rail antenna, and its wheel-rail system is shown in Figure 1(b). The azimuth operation of this kind of antenna has the characteristics of low speed and heavy

The associate editor coordinating the review of this manuscript and approving it for publication was Ladislau Matekovits.

load. In the use of antennas in the process of roller and track often have a great contact stress and wheel-rail friction coefficient, after long-term operation, its surface will appear wheel-rail wear, cracks, surface deformation and other damage [6], [7]. These damages will reduce its surface accuracy and service life [8], [9]. For example, the American GBT antenna and the German Effelsberg 100m antenna have different degrees of wear on the track after several years of operation, which affects the performance and service life of the wheel-rail [10], [11]; The 25m radio antenna in Sheshan, Shanghai, China, was found to have a large deformation of the track joints at the early stage of operation, which directly led to the reduction of the antenna's pointing accuracy [12].

The wheel-rail damage of large reflector antenna reduces its surface accuracy and directly affects the antenna pointing performance, so it is important to study the detection of damage to the wheel-rail surface. The GBT antenna in the U.S.A. was built and operated for a few years and had problems with wear on the surface of the substrate and wear plate, Anderson et al. investigated this issue, designed and manufactured a new component system, and updated the antenna component in 2007, which greatly improved the performance and service life of the azimuth orbit of the GBT antenna [13], [14]; Aiming at the mechanical behavior of the inclined joint track of GBT antenna and the fretting wear of the contact interface between wear-resistant plate and substrate, Juneja et al. simulated the rolling situation of the roller by using the moving load method, and analyzed the force by using the finite element method, which provided a reference for the design and transformation of the antenna wheel-rail [15]; In order to make the antenna have good pointing performance, Smith pointed out that attention must be paid to the wheel-rail design to make it have high hardness to withstand great contact pressure [16]; Guo et al. used Hertz contact theory and finite element method to analyze the stress of a radar wheel-rail type antenna mount, and did metallurgical analysis under the condition of satisfying the strength to determine the cause of cracks on the surface of the roller [17].

The above applications and theories of wheel-rail rolling contact are based on the traditional Hertzian contact theory, although the contact theory has made great progress so far, yet the method also has different degrees of limitations, which has been difficult to meet the needs of the development of antenna wheel-rail, and it cannot intuitively express the damage of antenna wheel-rail. Electromagnetic ultrasonic method with its unique advantages has become a new idea of antenna wheel-rail detection, compared with the previous wheel-rail contact theory, the method can be more intuitive to detect wheel-rail defects. Electromagnetic ultrasonic detection method with its no contact, no coupling medium, suitable for high temperature, detection efficiency and other advantages has gradually become the focus of research, the method is mainly used in train tracks, plates and pipes and other fields.

Although this method has been applied to the defect detection of other wheel-rails such as train wheel-rails, yet it has not been applied to the detection of antenna wheel-rails. Before this paper proposes this method for the detection of antenna wheel-rail, there is no real-time monitoring method for antenna wheel-rail in daily operation, and previous scholars have carried out monitoring and life prediction of the wheel-rail by analyzing the stress between the wheel-rail and the rollers, so this method has a significant research value for the antenna wheel-rail. This paper presents the method for detecting the surface characteristics of antenna wheel-rails using electromagnetic ultrasonic surface waves for the first time and focuses on illustrating the feasibility of the method through theoretical analyses and finite element simulations, and the design and validation of the experiments will be carried out on this basis.

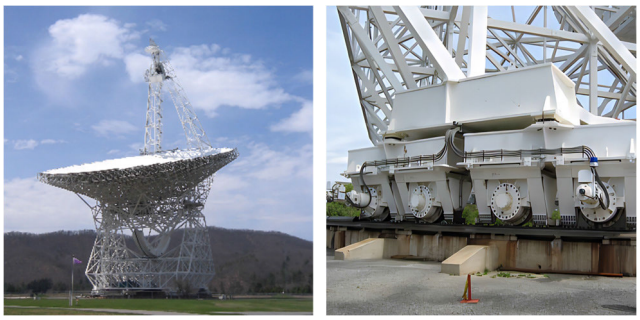
(a) (b)

FIGURE 1. Typical wheel-rail radio telescope. (a) GBT wheel-rail antenna; (b) wheel-rail system for GBT antenna.

II. PRINCIPLE AND METHOD OF ELECTROMAGNETIC ULTRASONIC TESTING

A. BASIC PRINCIPLES OF ELECTROMAGNETIC ULTRASONIC TESTING

The electromagnetic ultrasonic detection techniques dealt with in this paper all take electrical conductors as the measured objects, and their basic principles are based on electromagnetic induction phenomena, and the fundamental laws of macroscopic electromagnetic phenomena can be expressed very simply by Maxwell's equations [18], namely:

$$\nabla \times E = \frac{\partial B}{\partial t} \tag{1}$$

$$\nabla \times H = J + \frac{\partial D}{\partial t} \tag{2}$$

$$\nabla \times D = \rho \tag{3}$$

$$\nabla \times B = 0 \tag{4}$$

where E is the electric field strength; H is the magnetic field strength; D is the electric flux density; B is the magnetic flux density; J is the current density; ρ is the charge density.

In general, the electromagnetic properties of a medium under the action of an electromagnetic field can also be expressed by the following relation:

$$B = \mu H \tag{5}$$

$$J = \sigma E \tag{6}$$

$$D = \varepsilon E \tag{7}$$

where σ is the conductivity of the medium; ε is the dielectric constant of the medium; μ is the magnetic permeability of the medium.

Formulas (1)-(7) form the physical basis of the electromagnetic detection technique in this paper, and the solution of the electromagnetic detection problem can be found by combining the above formulas and by setting the boundary conditions of the specific model and applying the force.

B. ANTENNA WHEEL-RAIL ELECTROMAGNETIC ULTRASONIC INSPECTION MECHANISM

Electromagnetic ultrasonic detection mechanism is: in close proximity to the measured metal surface of the coil with high-frequency alternating current, the measured metal surface skin depth will produce a change in the electromagnetic field, and then in the surface will produce a same frequency of the induced eddy currents, the induced eddy currents in the applied bias magnetic field, resulting in the same frequency of the Lorentz force, which makes the specimen inside the point of the mass of the periodic vibration of the ultrasonic excitation, so as to detect the wheel-rail [19], [20].

Electromagnetic Acoustic Transducer (EMAT) is a non-contact transducer that can be used to detect damage on the surface of an antenna wheel-rail by means of electromagnetic coupling. EMAT is a non-contact transducer, which excites and receives ultrasonic waves in a conductor by electromagnetic coupling, and can easily excite various types of ultrasonic waves. Among them, the body wave can well detect the internal defects of the specimen, but there is a blind spot for surface and near-surface defects [21]; while the energy of the surface wave is mainly concentrated in the skinning depth of the specimen surface when it is propagated, which is suitable for the detection of surface opening defects of thick plates [22], [23]. The application in this paper is the detection of surface and near-surface defects by surface waves. EMAT is generally composed of a combination of a high-frequency coil, a biased magnetic field and a conductor under test. The components and principles are shown in Figure 2.

When the coil is passed through an alternating excitation current, a varying magnetic field is generated, and the alternating magnetic field induces eddy currents on the surface of the antenna wheel-rail, namely:

$$J_W = \nabla \times H \tag{8}$$

The Lorentz force is formed by the eddy currents in the wheel-rail under the action of the biased magnetic field, namely:

$$F_L = J_W \times B_P \tag{9}$$

where J_W is the induced eddy current; $H$is the alternating magnetic field strength; F_L is the Lorentz force; B_P is the bias

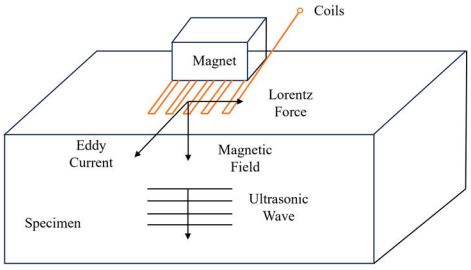

FIGURE 2. EMAT components and principles. EMAT consists of a magnet, coils and a test piece. When the coils pass through the excitation, an induced eddy current is generated on the surface of the test piece, which generates a Lorentz force inside the test piece under the action of a biased magnetic field, causing the mass to vibrate and thus generating an ultrasonic wave.

magnetic field strength. The Lorentz force causes the mass inside the wheel-rail to vibrate, which generates ultrasonic waves. When there are no defects, the ultrasound waves propagate along the surface, and the energy attenuation on the propagation path is very small during acoustic wave detection, it allows the ultrasound guided waves to propagate over long distances on the surface of the antenna wheel-rail or inside the antenna wheel-rail. When there are defects on the surface or near surface of the wheel-rail, the ultrasonic waves encountering the defects will undergo reflection phenomena and transmission phenomena, which involves the fluctuation problem of elastic dynamics, the solution of it is based on the fundamental solution of elastic dynamics. The research models in this paper are all based on 2-D model of the antenna wheel-rail, and the assumption of 2-D plane strain problem is made here. It is assumed that the defects in the detected 2-D model are actually defective grooves in the direction of the perpendicular plate cross-section. The following boundary integral equation for elastic dynamics can be introduced using the weighted residual method:

$$\frac{1}{2}\begin{bmatrix} u \\ v \end{bmatrix} + \int_{\Gamma} \begin{bmatrix} T_{11} & T_{12} \\ T_{21} & T_{22} \end{bmatrix} \begin{bmatrix} u \\ v \end{bmatrix} ds = \int \begin{bmatrix} U_{11} & U_{12} \\ U_{21} & U_{21} \end{bmatrix} \begin{bmatrix} t_x \\ t_y \end{bmatrix} ds \tag{10}$$

where U_{jk} and T_{jk} (j=1,2;k=1,2) are the elastic dynamics basis solutions, respectively represents the displacement and the surface force; Γ is the 2-D region boundary; u, v are the displacements in the X and Y directions; and t_x, t_y are the surface forces of F_L in the X and Y directions. According to the division of the boundary cells, the boundary equations with continuous integration over the whole boundary can be discretized into the following form:

$$\frac{1}{2}\begin{bmatrix} u \\ v \end{bmatrix} + \sum_{j=1}^{N} \int_{\Gamma_j} \begin{bmatrix} T_{11} & T_{12} \\ T_{21} & T_{22} \end{bmatrix} \begin{bmatrix} u \\ v \end{bmatrix} d\Gamma_j = \sum_{j=1}^{N} \int_{\Gamma_j} \begin{bmatrix} U_{11} & U_{12} \\ U_{21} & U_{22} \end{bmatrix} \begin{bmatrix} t_x \\ t_y \end{bmatrix} d\Gamma_j \tag{11}$$

where N is the total number of boundary cells.

Constant element is used in the boundary element program discussed in this paper. This element is geometrically represented as a straightness segment, and the physical quantity is

constant on each element. Although the calculation accuracy of constant elements is not as high as that of more complex linear and higher-order elements, according to the research of Cho and Rose [24], [25], the constant elements can also get better results in elastic wave problems.

If constant cells are used, the displacements and surface forces in the integral expressions contained in the boundary integral equations in discrete form can be referred to outside the integral sign, so that what needs to be solved is actually the integral of the underlying solution. The boundary integral in discrete form can be written as:

$$\frac{1}{2}u^i + \sum_{j=1}^{N} K_{ij}u^j = \sum_{j=1}^{N} G_{ij}t^j \tag{12}$$

where:

$$u^i = \begin{bmatrix} u \\ v \end{bmatrix}^i$$

$$t^j = \begin{bmatrix} t_x \\ t_y \end{bmatrix}^j$$

$$K_{ij} = \begin{bmatrix} \int_{\Gamma_j} T_{11} d\Gamma_j & \int_{\Gamma_j} T_{12} d\Gamma_j \\ \int_{\Gamma_j} T_{21} d\Gamma_j & \int_{\Gamma_j} T_{22} d\Gamma_j \end{bmatrix}$$

$$G_{ij} = \begin{bmatrix} \int_{\Gamma_j} U_{11} d\Gamma_j & \int_{\Gamma_j} U_{12} d\Gamma_j \\ \int_{\Gamma_j} U_{21} d\Gamma_j & \int_{\Gamma_j} U_{22} d\Gamma_j \end{bmatrix}$$

The unit number i is iterated within the unit number range $1 \leq i \leq N (i \in Z)$, and finally $2N$ equations are obtained, which are sorted as follows:

$$\boldsymbol{KU} = \boldsymbol{GT} \tag{13}$$

where:

$$K = \begin{bmatrix} K_{11} & K_{12} & \cdots & K_{1N} \\ K_{21} & K_{22} & \cdots & K_{2N} \\ \vdots & \vdots & & \vdots \\ K_{N1} & K_{N2} & \cdots & K_{NN} \end{bmatrix} + \frac{1}{2}I$$

$$G = \begin{bmatrix} G_{11} & G_{12} & \cdots & G_{1N} \\ G_{21} & G_{22} & \cdots & G_{2N} \\ \vdots & \vdots & & \vdots \\ G_{N1} & G_{N2} & \cdots & G_{NN} \end{bmatrix}$$

$$U = \begin{bmatrix} u^1 & u^2 & \cdots & u^N \\ v^1 & v^2 & \cdots & v^N \end{bmatrix}^T$$

$$T = \begin{bmatrix} t_x^1 & t_x^2 & \cdots & t_x^N \\ t_y^1 & t_y^2 & \cdots & t_y^N \end{bmatrix}^T$$

The solution of the elements of the coefficient matrices $\boldsymbol{K}$ and $\boldsymbol{G}$ needs to be discussed in two cases: 1) when $i \neq j$, $\boldsymbol{K}$ and $\boldsymbol{G}$ contain non-singular integrals, which can be solved directly by using the Gaussian product formula machine; 2) when $i = j$, the integrals in $\boldsymbol{K}$ and $\mathbf{G}$ have singularities at $r = 0$, which have to be dealt with in a special way.

After obtaining all the coefficients of the complex coefficient matrices $\boldsymbol{K}$ and $\boldsymbol{G}$, it is necessary to introduce the boundary conditions to obtain the system of linear equations for the final required solution. The hybrid boundary element model of a rectangular defective slot is shown in Figure 3. Ultrasonic waves propagate within the elastic flat plate interface, the upper and lower surfaces of the plate and the defects are free boundaries with a surface force of 0; the so-called virtual boundary is established a certain distance away from the left and right sides of the defects, and the virtual boundary and the free surfaces together form a closed model area; the appropriate frequency thickness product is selected according to the design, so that the single mode Lamb wave is incident from the left virtual boundary and interacts with the defects, part of the Lamb wave is reflected back to the left virtual boundary, and the other part of the Lamb wave is transmitted to the right virtual boundary.

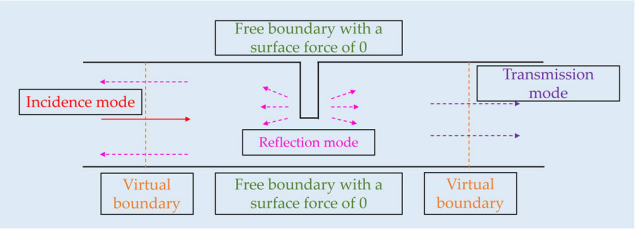

FIGURE 3. Boundary element action mechanism diagram. The upper and lower boundaries are zero stress boundaries and the left and right boundaries are virtual boundaries. The incident wave encounters the defect and generates reflected and transmitted waves.

When a symmetric or antisymmetric mode Lamb wave of a certain frequency thickness and order is input to the left virtual boundary of the model as an incident mode, the reflection and transmission modes obtained after the interaction of the incident mode and the defect may contain any mode that can exist at that frequency thickness, as determined by the dispersion curve. For a linear material, the total displacement of the left boundary should be the sum of the incident mode displacements and the displacements of all possible reflection modes, expressed as follows:

$$u^A = u^1 + u^{BS} \tag{14}$$

Similarly, the right boundary displacement should be the sum of the displacements of all possible transmission modes with the following expression:

$$u^A = u^{FS} \tag{15}$$

where u^A is the total displacement; u^{BS} is the reflection mode displacement; u^{FS} is the transmission mode displacement.

III. EXPERIMENT RESULTS AND DISCUSSION

A. ANTENNA WHEEL-RAIL AND DAMAGE FORMS

Large wheel-rail antenna azimuth wheel-rail is shown in Figure 4, its installation is generally divided into two kinds: splicing track technology and overall welding technology, different welding methods affect the service life of the track and pointing accuracy. Small aperture precision requirements are not high radio telescope usually use spliced track technology, segmented spliced track cost is low, but there are

shortcomings such as stress concentration at the welded joints, and the overall rigidity of the track is poor, it is prone to serious deformation under the action of a large load, which results in a decline in precision. The large-diameter, high-precision radio telescope track gradually adopts the overall welding technology, and the overall welding can reduce the welding deformation and shrink the weld, which in turn reduces the unevenness of the wheel-rail and improves the pointing accuracy of the wheel-rail. Most of the large antenna wheel-rail surface materials are made of forged 42CrMo and other structural steels, which are quenched and tempered by surface quenching and tempering, and have good contact strength and bending strength, but the carbon content and alloying elements in this type of material are high, which are prone to hot cracking, cold cracking, and delayed cracking.

Large wheel-rail type antenna seat frame is to use the friction between the roller and the track for transmission, so in the use of the antenna in the process of the roller and the track often have a great contact force between the wheel, and it will occur in the wheel-rail surfaces rolling contact fatigue, which is specifically manifested in the surface or subsurface micro-cracks, and then continued to expand. In actual engineering, the material surface or internal defects will greatly reduce the load threshold of rolling contact fatigue, is the most common cause of failure. The final form of rolling contact fatigue of the wheel-rail is the fracture of the wheel-rail material, which can seriously affect the normal operation of the antenna. Through the research and analysis of the working damage situation of wheel-rail of large reflector antennas in various countries, the wheel-rail of large reflector antennas generally experience the following types of damage on the surface [6], [7], [8], [9], [10], [11], [12], [13], [14]:

1) Wheel-rail wear: wheel-rail surface contact force is too large, the roller in the track after a long period of operation will produce track surface wear, reduce the precision of the wheel-rail;
2) Fatigue cracks: roller and track long-term role, a point of stress concentration, gradually sprouting cracks;
3) Wheel-rail corrosion: by the working environment as well as the influence of climate, the wheel-rail surface is corroded, which seriously affects the precision of the wheel-rail, thus affecting the normal work of the antenna.

B. CONSTRUCTION OF THE WHEEL-RAIL MODEL

This paper focuses on the 110-meter aperture fully movable radio telescope QTT as the research object, and the simulation model is established based on the QTT. The QTT is a sharp tool for future astronomical research in radio astronomy in China, and it is also the basic support and necessary condition for the breakthrough of cutting-edge technology, and it has a significant role for China's modern astronomy to enter into the ranks of the world's advanced. The track of the QTT is made of a number of single segment wheel-rails spliced together, with each segment of the size of the wheel-rail is 4000mm × 600mm × 200mm [26].

FIGURE 4. Azimuthal track for large wheel-rail antennas. The figure shows the profile of the antenna wheel-rail.

According to the parameters of the antenna wheel -rail, the ideal 3-D wheel-rail model is established. According to previous scholars' research on the antenna wheel-rail, the comprehensive research direction of this paper, considering the overall structural layout of the track, the track single-segment arc is shorter, in order to simplify the modeling process, ignoring the arc, and only a part of the wheel-rail single-segment is selected for modeling, which effectively simplifies the wheel-rail model [7], [27]. Figure 5 shows the schematic structure of the wheel-rail model.

In this paper, for the purpose of studying the surface defects of wheel-rail, orthogonal simulation experiments are used to establish a simplified 2-D wheel-rail model by intercepting the length and width of a single section of QTT wheel-rail to analyze the surface defects of wheel-rail from the perspective of multiple cross-sections. Among them, a simplified 2-D wheel-rail model with a length of 200 mm and a width of 10 mm was established by intercepting 1/20 of the cross-section of a single QTT wheel-rail in the length direction, and a simplified 2-D wheel-rail model with a length of 60 mm and a width of 10 mm was established by intercepting 1/10 of a single QTT wheel-rail in the width direction. Among them, the magnet remanent magnetization is 1.0T; the coil is 0.2mm wide and 0.035mm high, and the array arrangement is adopted.

Through the analysis the basic theory of electromagnetic ultrasonic detection, the research in this paper is mainly based on the Lorentz force mechanism, which is used to detect the surface defects of wheel-rails through the excitation of Lamb waves. Ultrasonic waves are generally divided into body waves and surface waves, and Lamb wave is a kind of surface waves. In electromagnetic ultrasonic detection according to the application object and system parameters, the body wave is generally used hundreds of kHz to tens of MHz; while the surface wave is generally used for low-frequency detection, usually a few hundred kHz to a few MHz. The Lamb wave used in this paper has dispersion characteristics, with the change of frequency will appear multimodal wave. According to the research object of this paper and the dispersion curve, the corresponding excitation frequency of 366.7e5Hz is selected to avoid the influence of clutter on the results. In this paper, a single probe is used to realize the excitation and reception of ultrasonic waves, the

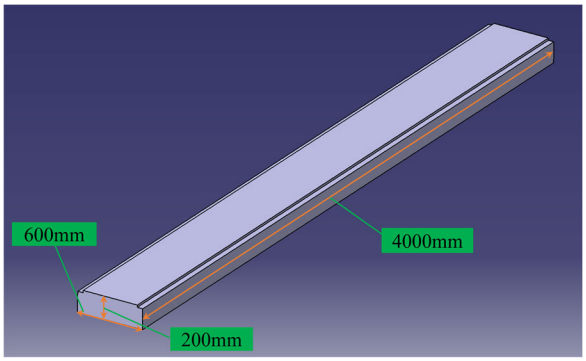

FIGURE 5. Simplified 3D model of the QTT wheel-rail. The picture shows a single section of QTT track, 4000mm long, 600mm wide and 200mm high.

probe is placed at the left end of the specimen, and the two directions of the cross-section of the probe are 60mm and 10mm away from the left end of the surface. The simplified 2-D model of the wheel-rail is shown in Figure 6(a) and (b).

C. ELECTROMAGNETIC ULTRASONIC EXCITATION PROCESS

In this paper, COMSOL Multiphysics finite element software is used as a carrier to study and analyze the established antenna wheel-rail model, which is divided into the following four phases:

1) Establish a simplified geometric model of the antenna wheel-rail. A low-reflection boundary is applied to the left and right boundaries of the model, and the reflections from the structural boundaries are neglected. The grid is divided into more than three layers in the skin depth, and other parts are appropriately coarsened;
2) Establish the electromagnetic field model. Set the appropriate step size and error in the transient solution to ensure the correctness and stability of the solution;
3) Establish the acoustic field model. This part uses the solid mechanics module to add the Lorentz force to realize the transformation of magnetic field to force field;
4) Multiphysics field coupling setup. The Lorentz force coupling setup is performed within the skin convergence depth of the specimen. The conversion of electric field-magnetic field-force field is realized by the above operations. The finite element simulation principle is shown in Figure 7.

In the process of solving the electromagnetic field differential equations, the boundary conditions are set for the measured conductor, with the top and bottom set as zero-stress boundaries and the left and right set as low-reflection boundaries. According to the excitation mechanism of electromagnetic ultrasound, an excitation is applied to the coil with an alternating current while neglecting the hysteresis effect and other secondary factors. The excitation current is shown in Figure 8, and it is in the form of:

$$I = cos\,(2 \times pi \times f_0 \times t) \times (1 - cos\,(2 \times pi \times f_0 \times t/5)) \times (t < 5 \times t_0) \times 10$$

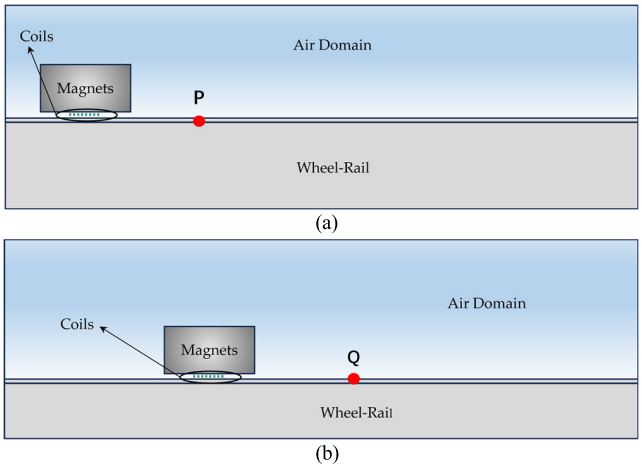

FIGURE 6. QTT wheel-rail 2D simplified model, the model includes wheel-rail, coils, magnets and air domain; (a) is the lengthwise section; (b) is the widthwise section.

D. SETTING OF WHEEL-RAIL SURFACE DAMAGE

For the possible defects on the surface of antenna wheel-rails, surface cracks, surface corrosion, surface wear and complete wheel-rails are modelled. Liu Suzhen and HD Jeong et al. used rectangular slots instead of actual crack defects of aluminum plates in the detection of unidirectional surface waves on tiny defects of aluminum plates, with the width of the crack defects being 0.2 mm and the depth being 0.3 mm. The relationship between the defects and the reflection coefficient was analyzed by simulation, and the fitted curves were plotted, which well express the function relationship between the depth of the cracks and the reflection coefficient [28], [29], [30]; Ren Xiaoke also used rectangular slots instead of crack damages and triangular slots instead of corrosion damages in the simulation, simulation used rectangular slots instead of crack damage and triangular slots instead of corrosion damage, and through the detection of cracks, it was found that the detection rate of open defects was high [31]. Drawing on the previous research ideas, this paper adopts rectangular groove equivalent to the actual wheel-rail crack damage in the simulation analysis [28], [29], [30]; corrosion usually corrodes downward from the middle point and then expands to both sides, so the simulation adopts inverted triangular groove equivalent to the actual wheel-rail corrosion damage [31]; the wear is usually a concave arc, and elliptical groove equivalent to the actual wheel-rail wear damage is adopted in the simulation [32]. By analyzing and comparing the model results without defects and the simulation results of several defects, the existence of defects and the location of defects can be judged more clearly and intuitively.

The modeling with or without defects is based on the selection of QTT wheel-rail, 1/20 of the length direction and 1/10 of the width direction of the QTT single-segment wheel-rail is taken as the object of study. In the distance from the left end face of the wheel-rail 160mm, from the

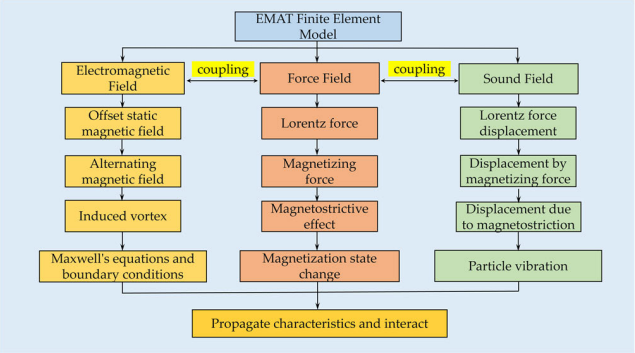

FIGURE 7. Principle of finite element simulation. The EMAT finite element mechanism includes the coupling of electromagnetic, force and sound fields.

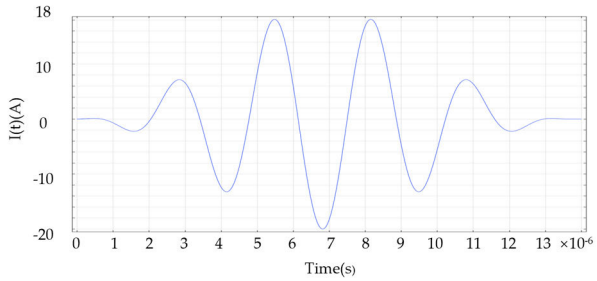

FIGURE 8. Excitation current signal waveform. The excitation wave is symmetric about the center. One period is 14e-6s and the peak current is 20A.

front face of 45mm was set up length, width and height of 1mm * 5mm * 2mm rectangular defect A, simulating weld or stress cracks and other defects in the shape of the sharper; In the consideration of the sharp defects, such as cracks, the antenna in practice, will be affected by the climate and the working environment and other influences, there are also a large number of defects due to the construction of defects or corrosion and other issues formed by the formation of pit defects, so also in the same location designed for 2mm * 5mm * 2mm triangular defect B; Finally, the comprehensive consideration of the wheel-rail surface forces are large, often occurring a certain amount of wear and slippage, therefore, in the same position of the half-axis of 3mm short half-axis of 2mm width of 5mm elliptical defect C on behalf of the wear and other injuries [33], [34]. The locations of the three defects are shown in Figure 9.

All three defects exhibit rectangular grooves in the width direction cross-section and rectangular grooves, triangular grooves and ellipses in the length direction cross-section. The simplified wheel-rail width cross-section defect model is shown in Figure 10(a) and the simplified wheel-rail length cross-section defect models are shown in Figure 10(b), (c) and (d).

E. WHEEL-RAIL DAMAGE DETECTION AND ANALYSIS

When the coil is excited by an alternating current source, an alternating electromagnetic field H is generated, and the magnetic induction of the alternating magnetic field is shown

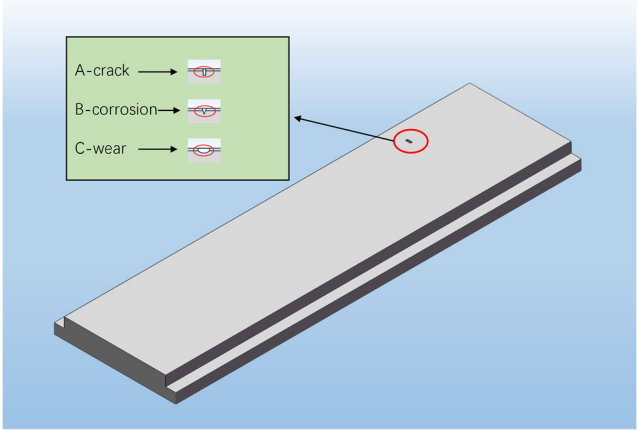

FIGURE 9. 3-D schematic diagrams of the three defects. ABC stands for three different kinds of defects.

in Figure 11(a). A biased magnetic field of $B_0 = 1.0T$ is added to the air, and the induced eddy currents are subjected to a Lorentz force in the X-direction due to the biased static magnetic field, the amplitude of which varies with the strength of the eddy currents as shown in Figure 11(b).

In this paper, orthogonal analysis is used to analyze the defects from different directions, and the width direction cross-section analysis is carried out first:

Figure12-(a), (b) show the 2-D cloud plots of the total displacement magnitude at T=1.7E-5s, and it is clear from the simulation results that the Lorentz force vibrates the internal plasmas of the wheel-rail, which generates ultrasonic waves. Regardless of the presence of defects, the modes of the ultrasonic waves propagating to the left side are the same and are not affected by the defects. When there is no defect, the mass displacement continues uniformly in one direction, the ultrasonic waves propagate along the surface of the wheel-rail without reflection or transmission, and there is very little energy attenuation in the propagation path during acoustic wave detection, which allows the ultrasonic guided waves to propagate over long distances on the surface of the antenna wheel-rail or internally. When there are defects on the surface or near the surface of the wheel-rail, the ultrasonic waves encountered by the defects will occur in the energy attenuation, as well as the phenomenon of reflection and transmission phenomena. From the formula (10)-(15), it can be seen that when there is a defect, the free boundary is changed, the displacement u, v and the size of the surface force t_x, t_y are changed, and the size of the displacement is also changed.

A point P (15, 10) is set on the surface of the two models, and Figure 12-(a), (b) shows the waveforms of the X-component of the displacement at point P for the two models.

Figure 13-(a) shows the waveform of the displacement at point P in the absence of defects, and only the first wave packet can be observed as a direct wave. Figure 13-(b) shows the displacement waveform of point P with a crack defect, the first wave packet is a direct wave and the second wave

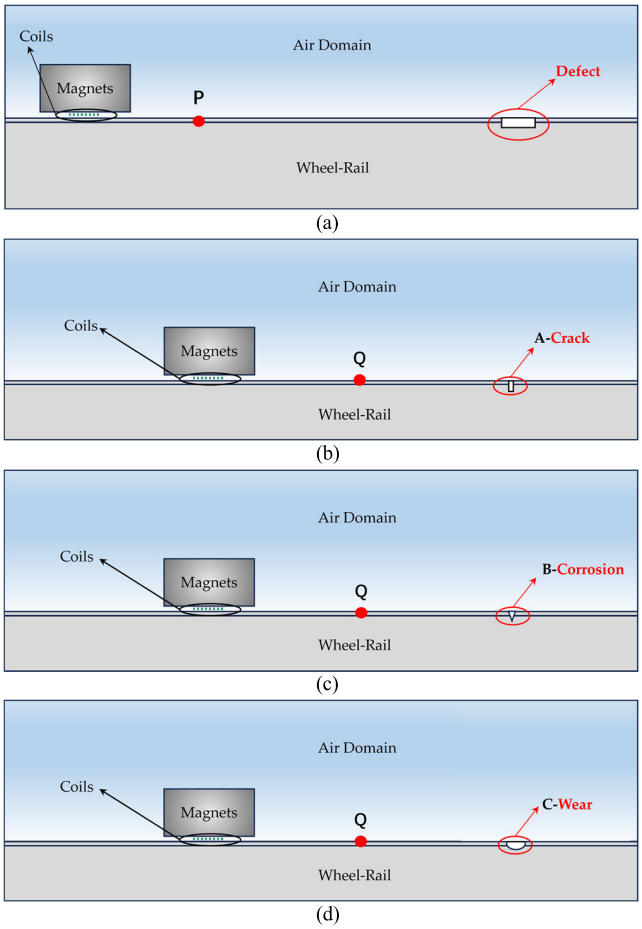

FIGURE 10. Simplified model of wheel-rail for three defects. (a) Modeling of width-direction cross-section defects of wheel-rail; (b) Modeling of crack defects in the lengthwise section of wheel-rail; (c) Modeling of corrosion defects in lengthwise sections of wheel-rail; (d) Modeling of wear defects in the lengthwise section of wheel-rail. ABC stands for three different kinds of defects.

packet is a reflected wave reflected back through the defect. The approximate position of the defect can be calculated by the time difference between the defective wave and the direct wave at point P. According to Figure 13-(b), the time difference between the direct wave and the defective wave can be read out to be 1.9E-5s, and according to the wave speed of ultrasonic wave in the aluminum plate is 3100m/s, the distance traveled by the ultrasonic wave is calculated to be L, two times of the distance of the defect from point P.

$$L = 3100 \times 1.9 \times 10^{-5} = 0.589\text{m} = 5.89\text{cm}$$

Since the actual distance traveled is 6.0 cm, the detection error is obtained as:

$$\frac{6.0 - 5.89}{6.0} = 1.8\%$$

After analyzing the width direction section, the length direction section is then analyzed:

Figure 14-(a), (b), (c) and (d) shows the 2-D cloud plots of the total displacement magnitude of the four simplified models of the wheel-rail at the moment of T=3.8E-5s. It is clear

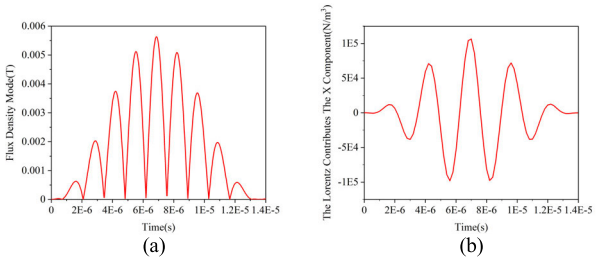

FIGURE 11. A graph of the magnetic induction and Lorentz force waveforms over one cycle. (a) Waveform of the magnetic induction of an alternating magnetic field; (b) Lorentz force waveform.

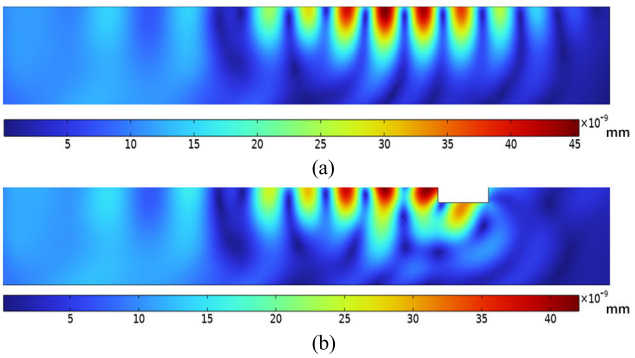

FIGURE 12. 2-D cloud plot of total displacement of two simplified models of wheel-rail at T=1.7E-5s. (a) No-Defect wheel-rail model displacement; (b) Defect wheel-rail model displacement.

from the simulation results that the Lorentz force vibrates the internal plasmas of the wheel-rail, thus generating ultrasonic waves. Regardless of the presence of defects, the modes of the ultrasonic waves propagating to the left side are the same and are not affected by the defects. When there is no defect in the wheel-rail, the mass displacement continues uniformly in one direction, the ultrasonic waves propagate along the surface of the wheel-rail without reflection or transmission, and there is very little energy attenuation in the propagation path during acoustic wave detection, which allows the ultrasonic guided waves to propagate over long distances on the surface of the antenna wheel-rail or internally. When there are defects on the surface or near the surface of the wheel-rail, ultrasonic waves encountered by the defects will occur in the attenuation of energy, as well as the phenomenon of reflection and transmission phenomena. From the formula (10)-(13), when there is a defect, the free boundary changes, the displacement u, vand surface force t_x, $t_y$size changes, the displacement size also changes; Figure 14-(b), (c) and (d) displacement amplitude relative to 14-(a) displacement amplitude increased a lot, this is because ultrasonic waves encountered defects after the reflection of the superposition of the result, and the deeper the depth of the defect the greater the amplitude of the displacement. Combined with formulas (14)-(15), it can be seen that the total displacement of the left boundary of the defect is the sum of the displacements of the incident mode and all possible reflection modes, when the ultrasonic wave encounters the defect, the energy of the left boundary of the defect increases and is usually larger than the energy

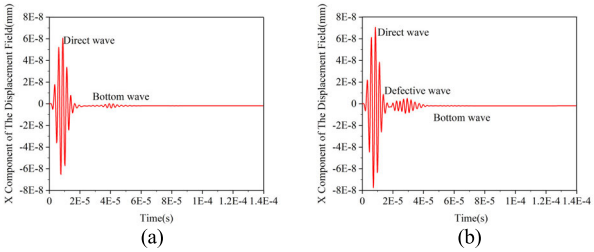

FIGURE 13. Waveform of the displacement of point P. (a) is the waveform of the defect-free model; (b) is the waveform of the defective model.

of the other positions of the wheel-rail, in which the stress concentration is easy to occur, which can easily lead to the damage of the wheel-rail; the total displacement of the right boundary is the sum of the displacements of all possible transmission modes, and the energy is gradually attenuated with the increase of the propagation distance.

A point Q (90, 10) is set on the surface of each model, and Figure 15-(a), (b), (c) and (d) show the waveforms of the displacement X component at point Q under the four models. It is generally recognized that the reflected wave between the start wave (direct wave) and the bottom wave is a defective wave. When there is no defect on the surface of the wheel-rail, there is only the beginning wave and the bottom wave; when there is a small defect on the surface of the wheel-rail, there is a defect in addition to the beginning wave and the bottom wave, and the defect wave and the bottom wave exist at the same time.

Figure 15-(a) shows the displacement waveform of point Q without defects, only the first wave packet can be observed as a direct wave with an amplitude of 5.4 × 10.8mm, and the second and third wave packets are the primary bottom wave and the secondary bottom wave.

Figure 15-(b) shows the displacement waveform of point Q under the crack defect, the first wave packet is the direct wave with an amplitude of 5.3 × 10.8mm, the second wave packet is the reflected wave reflected back through the defect with an amplitude of 2.3 × 10.8mm, and the wave packet after the defect wave is the bottom wave. The approximate position of the defect can be calculated by the time difference between the defect wave and the direct wave at point Q. According to Figure 15-(b), the time difference between the direct wave and the defect wave can be read out as 4.6E-5s, and according to the wave speed of ultrasonic wave in the aluminum plate is 3100m/s, the distance traveled by the ultrasonic wave is calculated to be L, it is two times of the distance of the defect from point Q.

$$L = 3100 \times 4.6 \times 10^{-5} = 0.1426\text{m} = 14.26\text{cm}$$

Since the actual distance traveled is 14.1 cm, the detection error is obtained as:

$$\frac{14.26 - 14.1}{14.1} = 1.1\%$$

Figure 15-(c) shows the displacement waveform of point Q under the corrosion defect, the first wave packet is the direct wave with the amplitude of 5.2 × 10.8mm, the second wave packet is the reflected wave reflected back through the defect with the amplitude of 1.4×10.8mm, and the wave packet after the defect wave is the bottom wave. The approximate position of the defect can be calculated by the time difference between the defect wave and the direct wave at point Q. According to Figure 15-(c), the time difference between the direct wave and the defect wave can be read out as 4.6E-5s, and according to the wave speed of ultrasonic wave in the aluminum plate is 3100m/s, the distance traveled by the ultrasonic wave is calculated to be L, it is two times of the distance of the defect from point Q.

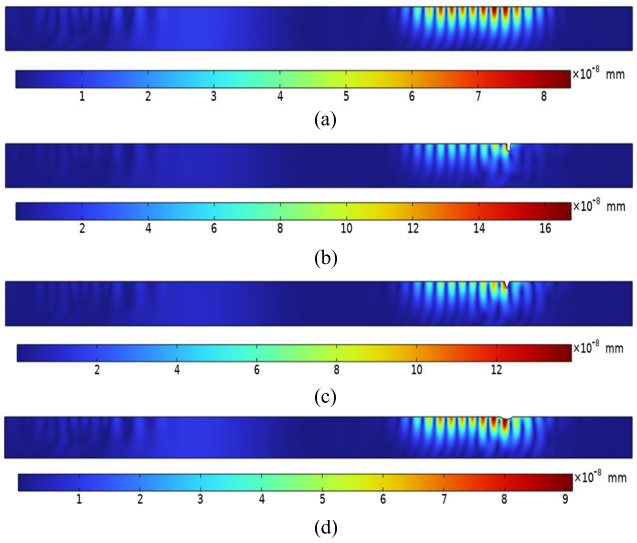

FIGURE 14. 2-D cloud plot of total displacement of four simplified models of wheel-rail at T=3.8E-5s. (a) No-Defect wheel-rail model displacement; (b) Crack Defect wheel-rail model displacement; (c) Corrosion Defect wheel-rail model displacement; (d) Wear Defect wheel-rail model displacement.

$$L = 3100 \times 4.6 \times 10^{-5} = 0.1426\text{m} = 14.26\text{cm}$$

Since the actual distance traveled is 14.2 cm, the detection error is obtained as:

$$\frac{14.26 - 14.2}{14.2} = 0.4\%$$

Figure 15-(d) shows the displacement waveform of point Q under the wear defect, the first wave packet is the direct wave with the amplitude of 5.4 × 10.8mm, the second wave packet is the reflected wave reflected back through the defect with the amplitude of 0.8 × 10.8mm, and the wave packet after the defect wave is the bottom wave. The approximate position of the defect can be calculated by the time difference between the defect wave and the direct wave at point Q. According to Figure 15-(d), the time difference between the direct wave and the defect wave can be read out as 4.5E-5s, and according to the wave speed of ultrasonic wave in the aluminum plate is 3100m/s, the distance traveled by the ultrasonic wave is calculated to be L, it is two times of the distance of the defect from point Q.

$$L = 3100 \times 4.5 \times 10^{-5} = 0.1395\text{m} = 13.95\text{cm}$$

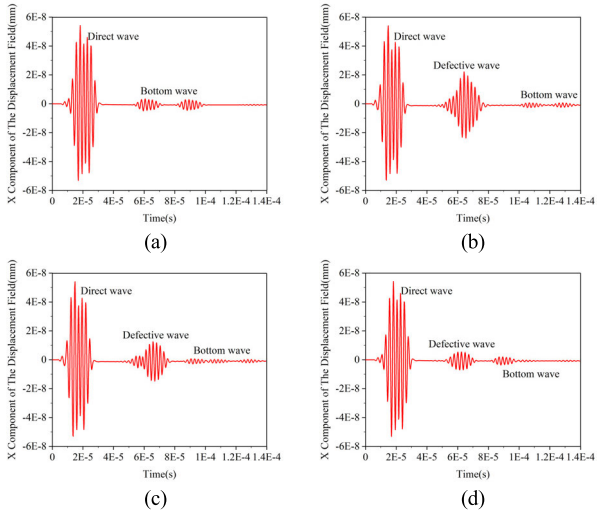

FIGURE 15. Waveform of the displacement of point Q. (a) No-Defect wheel-rail model displacement; (b) Crack Defect wheel-rail model displacement; (c) Corrosion Defect wheel-rail model displacement; (d) Wear Defect wheel-rail model displacement.

Since the actual distance traveled is 14.1 cm, the detection error is obtained as:

$$\frac{13.95 - 14.1}{14.1} = 1.0\%$$

It can be seen that the electromagnetic ultra method is effective in detecting and localizing surface defects in wheel-rails.

By comparing the three diagrams of 15-(b), (c) and (d), it can be seen that Figure 15-(b) is the waveform diagram of crack damage model on the surface of the wheel-rail, and its defective echo is higher, with more peaks, sharp and steep; Figure 15-(c) is the waveform diagram of corrosion damage model on the surface of the wheel-rail, and its defective echo is broader, steeper and straighter, and there is obvious dendritic shape; Figure 15-(d) is the waveform diagram of abrasion damage model on the surface of the wheel-rail, and its defective echo is lower, with broader and sawtooth-shaped waveforms. Comparison of the three kinds of defective waves shows that with the increase of defect width, the reflected wave packet width also increases; with the increase of defect depth, the reflected wave packet amplitude also increases. Therefore, it can be concluded that when the width of the reflected wave packet is wider, it means that the defect width is longer, which affects the duration of the reflected wave; when the amplitude of the reflected wave is smaller, it means that the depth of the defect is shallower, and the surface wave can be easily transmitted from the shallower defect; when the depth of the defect is increased, the amplitude of the reflected wave is increased, which means that the deeper the defect is, the easier it is for the surface wave to be reflected back.

In the antenna wheel-rail surface defect detection, not only the qualitative and localization analysis of defects, the quantitative analysis of defects is also crucial. Since the deeper the defect, the greater the amplitude of the reflected signal; the longer the defect, the greater the reflected signal, so according

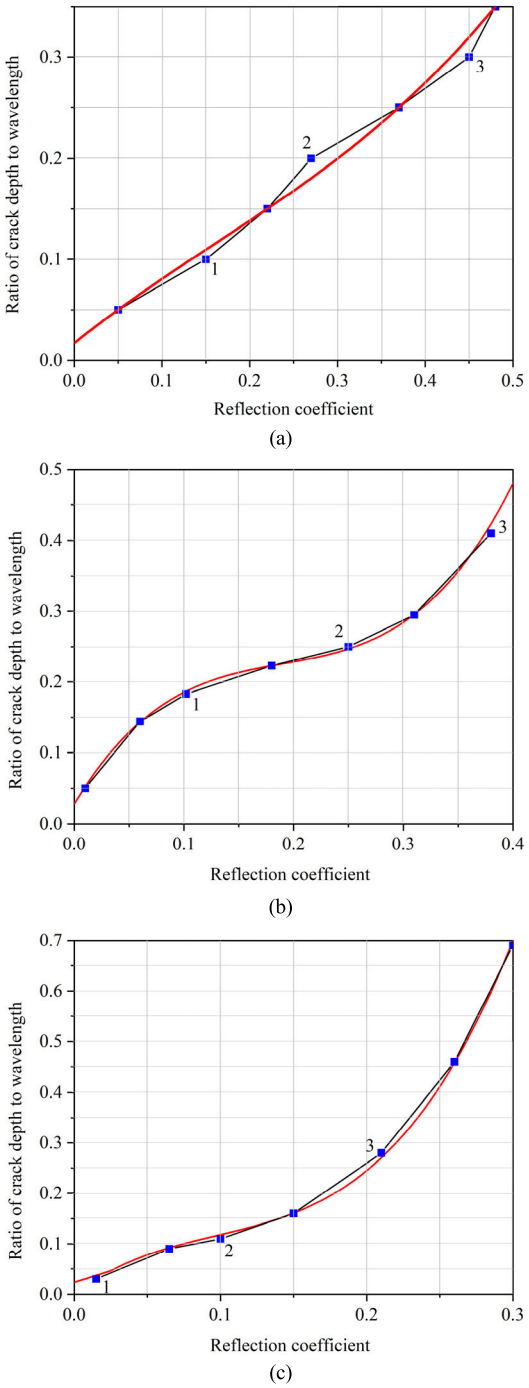

FIGURE 16. The curves of reflection coefficient versus flaw depth. The blue point is the calculation point, and the red line is the fitting curve. (a) Fitting curve for crack damage; (b) Fitting curve for corrosion damage; (c) Fitting curve for wear damage.

to the amplitude of the reflected wave from the depth and length of the two directions of the quantitative analysis of defects.

In order to eliminate the effect of different incident signals and detection positions in each experiment, the reflection coefficient R was defined:

$$R = \frac{\text{amplitude of defective reflected wave signal}}{\text{amplitude of incident signal}}$$

TABLE 1. Comparison of defective deviation points.

Point	Crack	Corrosion	Wear
1	0.0095mm	0.00386mm	0.02277mm
2	0.0280mm	0.00303mm	0.03081mm
3	0.0192mm	0.01343mm	0.01340mm

TABLE 2. Detection accuracy of different defects.

	Crack	Corrosion	Wear
Detection Accuracy	0.13776mm	0.22755mm	0.19065mm

The reflection coefficient R is the ratio of the amplitude of the reflected wave signal from a defect to the amplitude of the incident wave, which varies with the depth and length of the defect. In this paper, three antenna wheel-rail surface defect models designed above are selected for quantitative study. Simulation experiments are carried out for defects of the same length and different depths, and the discrete points of heir reflection coefficients are taken for curve fitting. A third-order function is fitted with the reflection coefficient as the independent variable and the defect echo to wavelength ratio as the dependent variable. Formulas 16, 17, 18 and Figures 16-(a), (b) and (c) show the fitted function and fitted curves for the three defects.

$$y = 1.60x^3 - 0.78x^2 + 0.699x + 0.0168 \quad (16)$$

$$y = 21.15x^3 - 12.06x^2 + 2.57x + 0.02775 \quad (17)$$

$$y = 52.96x^3 - 15.41x^2 + 2.187x + 0.02325 \quad (18)$$

where formula 16 is the fitting function for crack damage; formula 17 is the fitting function for corrosion damage; and formula 18 is the fitting function for wear damage.

The quantitative analysis of the three defects at different depths leads to Figure 16-(a), (b) and (c). Comparison of the three figures shows that most of the points are on the fitted curves and only individual points deviate from the fitted curves. The magnitude of the deviation for the three different defects is shown in Table 1:

As can be seen from the deviation values of different defects at each point in Table 1, the fitting curves of vertical defects such as cracks and corrosion are more accurate than those of elliptical defects such as abrasion, which indicates that the method is more sensitive to the detection of defects that are perpendicular to the wheel-rail or at a larger angle to the surface of the wheel-rail.

By comparing Formulas 16, 17 and 18, it can be seen that when the reflection coefficient R is 0, the ratio of the three kinds of defects to the wavelength is 0.0168, 0.02775 and 0.02325, and the sizes of the different defects at this moment can be calculated to be 0.13776 mm, 0.22755 mm and 0.19065 mm. The sizes of the three kinds of different defects correspond to the detection accuracy of the three kinds of defects by the method. The detection accuracy of the three defects is shown in the table 2.

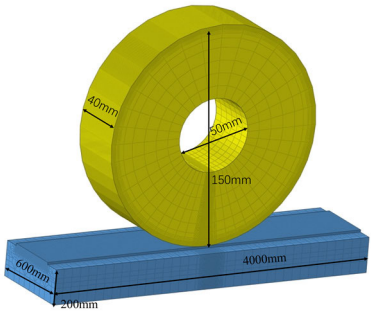

FIGURE 17. Hertz theory simulation model diagram and dimensions for each section.

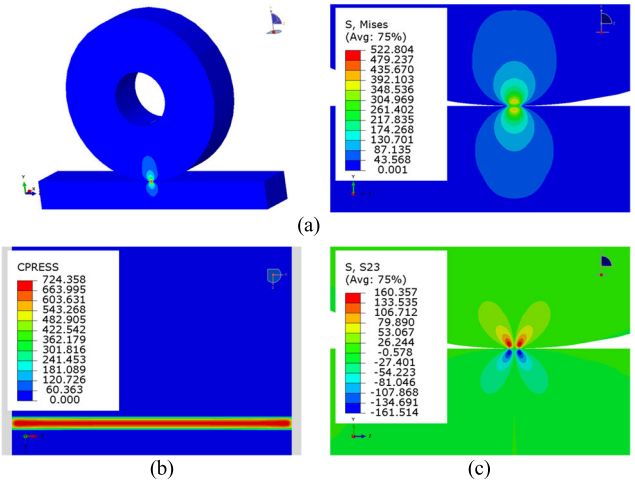

FIGURE 18. Non-invasive modeling results (a) The pattern for Mises stress; (b) the pattern for contact pressure; (c) the pattern for maximum shear stress.

Although the defects can be quantitatively analyzed by fitting the function, but in the process are based on a single variable for research, which is only a preliminary quantitative method. In order to obtain a more accurate functional relationship, subsequent multivariate simultaneous research is needed, and also different sizes of defective echoes can be unified into a single dataset, which can be used for the detection and prediction of various damages through neural networks.

F. COMPARATIVE ANALYSIS BASED ON CONVENTIONAL HERTZ THEORY AND ELECTROMAGNETIC ULTRASOUND TECHNIQUES

Based on the traditional Hertzian contact theory analysis method, the research model is constructed according to the simulation process in the previous section, and the model without defects is shown in Figure 17.

After establishing the model, the whole model is meshed, especially the mesh of the contact spot area of the wheel-rail and roller is subdivided to ensure the accuracy of the results. According to the weight of the antenna and the reasonable bearing of the track, the single wheel load is set to 4×10^5 kg

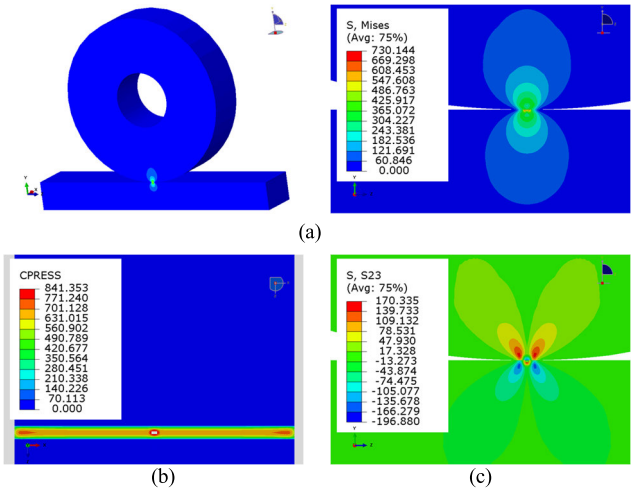

FIGURE 19. Crack damage modeling results (a) The pattern for Mises stress; (b) the pattern for contact pressure; (c) the pattern for maximum shear stress.

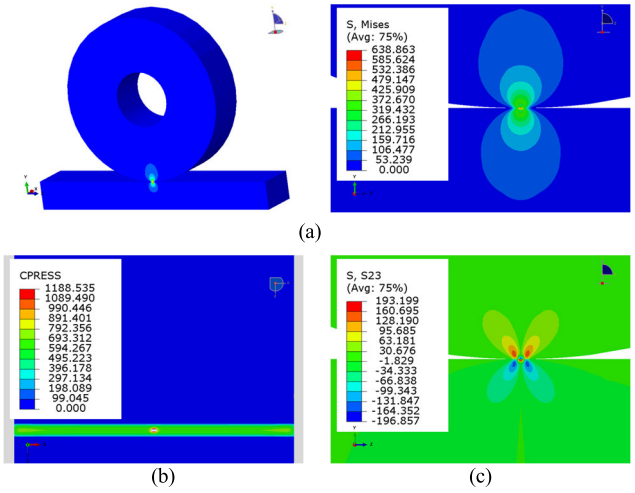

FIGURE 20. Corrosion damage modeling results (a) The pattern for Mises stress; (b) the pattern for contact pressure; (c) the pattern for maximum shear stress.

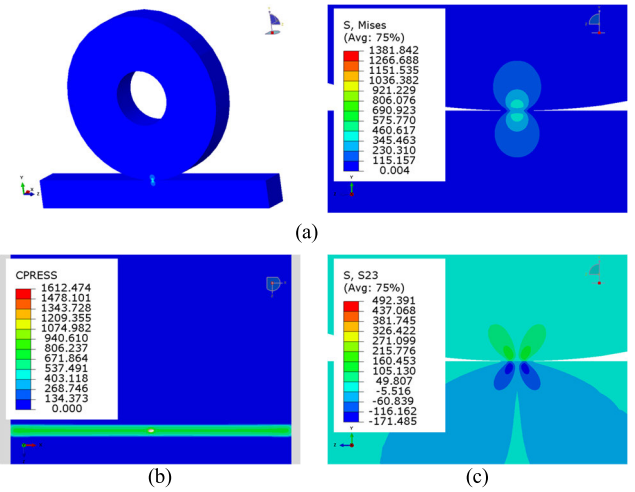

FIGURE 21. Wear damage modeling results (a) The pattern for Mises stress; (b) the pattern for contact pressure; (c) the pattern for maximum shear stress.

TABLE 3. The magnitude of different model forces.

	Mises Stress (/MPa)	Contact Pressure (/MPa)	Shear Stress (/MPa)
non-destructive	522.804	724.358	160.357
Crack	730.144	841.353	170.335
Corrosion	638.863	1188.535	193.199
Wear	1381.842	1612.474	492.391

TABLE 4. Comparison of the two methods.

	Electromagnetic Ultrasound Technology	Conventional Hertzian Theory
Structure Composition	Wheel-rail	Wheel-rail and rollers
Operating Method	Simple operation without contact	Requires contact and is complex to operate
Defect Detection	Defects can be detected	Defects can be detected
Defect Analysis	Defects can be analyzed visually	Indirect analysis of defects

to ensure the safety of the actual working conditions. The centralized load is applied on the axle wheel, and considering the influence of the self-weight of the track, its bottom surface is set to be fully constrained, and the rollers are constrained to the transverse degrees of freedom to avoid transverse slip.

On the premise of previous research, three separate models with different injuries were constructed on the basis of this model, in which the size and location of the injuries were constant. Based on the traditional Hertz theory, considering the static working condition of the antenna roller located on the wheel-rail, finite element analysis is carried out on the model with or without damage. The force cloud diagram of the wheel-rail is shown in Figure18, 19,20 and 21.

Figures 18, 19, 20, and 21 show the 2D cloud plots of Mises stresses, contact point pressures, and shear stresses for the contact between the roller and the wheel-rail with and without the damage model studied in the previous section. The magnitude of the different forces for each model is shown in Table 3 (in MPa):

As can be seen from Table 3, when there is damage on the surface of the wheel-rail, the Mises stress between the roller and the wheel-rail, as well as the pressure and shear stress at the contact point, increase significantly, which indicates that when there is a defect, the force between the roller and the wheel-rail increases and there is a concentration of stress in the vicinity of the damage. By comparing the results of non-destructive and different defects, it can be seen that for defects perpendicular to the surface of the wheel-rail, such as cracks, the increase in force is not particularly significant; however, for defects at an angle to the surface of the wheel-rail, such as corrosion and abrasion, it can be seen that the change in force is significant. This indicates that the damage at an angle to the surface of the wheel-rail is more likely to cause problems with the wheel-rail.

Through the analysis of Figure 18, 19, 20 and 21, the contact stress between the wheel-rail and the roller can only be visually analyzed, and although the presence of defects can be seen, but it is not possible to qualitatively as well as locationally quantitatively analyze the defects through the resultant data. The comparison between the traditional Hertzian theory method and the method proposed in this paper is shown in Table 4:

As can be seen through Table 4, although the two methods have different bases for judging defects, they can both determine the existence of defects. Compared with the electromagnetic ultrasonic method proposed in this paper, the traditional Hertz theory method has a complex structure, needs to analyze the roller and the wheel-rail at the same time, needs to be coupled and complicated operation, can only analyze the damage on the surface of the wheel-rail through the force between the roller and the wheel-rail, and is more indirect to the judgment of defects. Moreover, it cannot analyze the defects qualitatively, locally and quantitatively. Hertz theory method is more suitable for the analysis of the force between the roller and the wheel-rail, but for the detection of defects in practice the method proposed in this paper is more advantageous.

Compared with the electromagnetic ultrasonic detection method proposed in this paper, the traditional Hertz theory method can only analyze the surface damage of the wheel-rail through the force and deformation between the wheel-rail, which is more indirect to determine the existence of defects. However, the method in this paper can not only locate, quantify and qualify the damage, but also easy to operate in practical applications.

Simulation results show that electromagnetic ultrasonic surface waves can well identify and locate the tiny defects on the surface of the antenna wheel-rail; The location of the defect is calculated by the time difference between the defect wave and the direct wave; the relationship between the reflection coefficient and the crack depth and length can be utilized to quantify the defect more accurately. Through the method of orthogonal experiment, the defects can be effectively localized and quantitatively analyzed in XYZ 3-D direction. Subsequently, further optimization of the model and parameters is needed to obtain more accurate defect information. In this paper, the electromagnetic ultrasonic detection method of antenna wheel-rail surface defects is proposed for the first time, and the design and validation of the experiments will be carried out on this basis.

IV. CONCLUSION

This paper concludes and analyses the azimuthal wheel-rail surface damage forms of large wheel-rail type antennas, and proposes the use of electromagnetic ultrasonic nondestructive testing methods to detect antenna wheel-rail damage for the first time. Different types of defects are simulated using a combination of theoretical analysis and numerical simulation. Simulation results show that the electromagnetic ultrasonic surface waves can well identify and locate the small defects on the surface of the antenna wheel-rail; through the relationship between the reflection coefficient and the depth of the crack can be more accurately quantify the depth of the defects, which provides a basis for quantitative detection of small defects on the surface of the antenna wheel-rail; through the analysis of the signal waveform, it can be clearly seen that the difference between the different types of defects, which provides the basis for the classification of the identification of defects. The method can provide an important reference for the study of wheel-rail damage detection of large reflector antennas.

This paper focuses on the feasibility of the wheel-rail damage detection method for large reflector antennas, verifies the feasibility of the design study through experiments, and further analyzes the defects quantitatively and qualitatively. On the basis of the research in this paper, the body wave can also be used to detect the internal damage of the antenna wheel-rail as well as to judge the damage through the neural network method in the subsequent research. After determining the detection accuracy of various defects, the size of the defects and the antenna wheel track pointing error can be subsequently studied together by measuring the unevenness caused by different defects.

REFERENCES

[1] I. de Pater, E. M. Molter, and C. M. Moeckel, "A review of radio observations of the giant planets: Probing the composition, structure, and dynamics of their deep atmospheres," *Remote Sens.*, vol. 15, no. 5, p. 1313, Feb. 2023.

[2] N. Wang, "Xinjiang Qitai 110 m radio telescope," *Scientia Sinica Phys., Mechanica Astronomica*, vol. 44, no. 8, pp. 783–794, Jul. 2014.

[3] Q. Xu, H. Wen, N. Wang, and L. Li, "Development challenges for the Xinjiang 110 m radio telescope (QTT) high accuracy panel structures," *Scientia Sinica Phys., Mechanica Astronomica*, vol. 47, no. 5, May 2017, Art. no. 059502.

[4] Y.-L. Gao, P. Wang, G.-Y. Tian, S.-S. Hao, and L.-H. Xiong, "High-speed online inspection techniques of rail crack defects based on electromagnetic principle," *NDT*, vol. 34, no. 12, pp. 1–11, 2012.

[5] Y. Ban, S. Feng, G. A. E. Vandenbosch, C. Wang, J. Zhang, B. Duan, and W. Wang, "Calculation of the best fit subreflector and its application in eliminating the harmless error of deformed large subreflectors," *IEEE Trans. Antennas Propag.*, vol. 68, no. 8, pp. 5855–5863, Aug. 2020.

[6] N. Wang, Q. Xu, and J. Ma, "The Qitai radio telescope," *Sci. China Phys. Mech. Astron.*, vol. 66, no. 8, 2023, Art. no. 289512.

[7] S.-K. Wang, D.-Q. Kong, and Z.-P. Chen, "Contact in wheel-rail systems for large radio telescopes: A review," *Astronomical Res. Technol.*, vol. 11, no. 1, pp. 27–33, 2014.

[8] X. Liu, Y. Aili, B.-B. Xiang, C.-S. Wang, Q. Xu, and J. Wang, "Analysis and correction of the influence of the track irregularity on antenna pointing," *Acta Astronomica Sinica*, vol. 58, pp. 49–59, Jul. 2017.

[9] J. Wu and B. Wang, "Influence of track irregularity on the pointing accuracy for large reflector antenna," *J. Terahertz Sci. Electron. Inf. Technol.*, vol. 15, no. 4, pp. 634–639, 2017.

[10] F. W. Kan and J. Antebi, "Slip and wear in multilayer azimuth track systems," *Proc. SPIE*, vol. 5495, pp. 549–587, Sep. 2004.

[11] R. M. Prestage and R. J. Maddalena, "The Green Bank Telescope: Current status and early results," *Proc. SPIE*, vol. 4837, pp. 944–953, Feb. 2003.

[12] J.-X. Gu, "Research on the antenna pointing error of 25 m radio telescope," *Ann. ShangHai Observatory Academia Sinica*, vol. 15, pp. 205–211, Jan. 1994.

[13] R. Anderson, A. Symmes, and D. Egan, "Replacement of the Green Bank Telescope azimuth track," *Proc. SPIE*, vol. 63, no. 14, pp. 3026–3030, 2008.

[14] A. Symmes, R. Anderson, and D. Egan, "Improving the service life of the 100-meter Green Bank Telescope azimuth track," *Proc. SPIE*, vol. 7012, pp. 1225–1236, Jul. 2008.

[15] G. Juneja, F. W. Kan, and J. Antebi, "Update on slip and wear in multi-layer azimuth track systems," *Proc. SPIE*, vol. 6273, pp. 368–378, Jul. 2006.
[16] D. R. Smith, "Achievable alignment accuracy and surface hardness of a large welded azimuth track," *Proc. SPIE*, vol. 6273, pp. 322–330, Jul. 2006.
[17] H.-W. Guo, "Analysis of surface crack on wheel of a rail type pedestal of radar," in *Proc. Electron. Machinery Microw. Struct. Technol. Conf.*, 2008, pp. 270–272.
[18] P. Y. Huray, *Maxwell's Equations*. Hoboken, NJ, USA: Wiley, 2011.
[19] S.-L. Huang, *Electromagnetic Ultrasonic Guided Wave Theory and Application*. China: Tsinghua Univ. Press, 2013.
[20] R. Marijan, *Conservation Laws and Open Questions of Classical Electrodynamics*. Singapore: World Scientific, 1990.
[21] C. Pei, T. Fukuchi, H. Zhu, K. Koyama, K. Demachi, and M. Uesaka, "A study of internal defect testing with the laser-EMAT ultrasonic method," *IEEE Trans. Ultrason., Ferroelectr., Freq. Control*, vol. 59, no. 12, pp. 2702–2708, Dec. 2012.
[22] S. Wang, L. Kang, Z. Li, G. Zhai, and L. Zhang, "3-D modeling and analysis of meander-line-coil surface wave EMATs," *Mechatronics*, vol. 22, no. 6, pp. 653–660, Sep. 2012.
[23] Z.-G. Zhang, P.-W. Que, and H.-M. Lei, "Electromagnetic transducers for surface wave generation and their electroacoustic characteristics," *Tech. Acoust.*, vol. 25, pp. 119–123, 2006.
[24] Y. Cho and J. L. Rose, "A boundary element solution for a mode conversion study on the edge reflection of Lamb waves," *J. Acoust. Soc. Amer.*, vol. 99, no. 4, pp. 2097–2109, Apr. 1996.
[25] Y. Cho and J. L. Rose, "An elastodynamic hybrid boundary element study for elastic guided wave interactions with a surface breaking defect," *Int. J. Solids Struct.*, vol. 37, no. 30, pp. 4103–4124, Jul. 2000.
[26] Q. Xu and G.-X. Hu, "Prediction of multi-layer and multi-pass welding angle deformation under gravity bending moment of QTT antenna orbit," *Trans. Chtna Weld. Inst.*, vol. 41, no. 8, pp. 10–13, 2020.
[27] H.-Q. Shi, Q. Xu, N. Wang, and Z.-J. Wang, "Finite element analysis of wheel-on-track rolling contact for large aperture radio telescope," *Astronomical Res. Technol.*, vol. 19, no. 2, pp. 95–102, 2022.
[28] S.-Z. Liu, S. Dong, Z. Fang, and C. Zhang, "Tiny defect detection of aluminium plate by ultrasonic unidirectional surface electromagnetic wave," *Tech. Acoust.*, vol. 38, no. 3, pp. 290–295, 2019.
[29] S.-Z. Liu, S.-J. Wang, C. Zhang, L. Jin, and Q.-X. Yang, "Simulation analysis of electromagnetic acoustic surface wave of steel plate and quantitative defect detection," *Trans. China Electrotechnical Soc.*, vol. 35, no. 1, pp. 97–105, 2020.
[30] J. Rose, H. Shin, and H. Jeong, "Detection of defects in a thin steel plate using ultrasonic guided wave," *J. Korean Soc. Nondestruct. Test.*, vol. 18, no. 6, pp. 445–454, 2000.
[31] X.-K. Ren and J. Li, "Simulation research on electromagnetic acoustic NDT by ANSYS," *Electron. Meas. Technol.*, vol. 31, pp. 26–28, Jul. 2008.
[32] N. Bosso, M. Magelli, and N. Zampieri, "Simulation of wheel and rail profile wear: A review of numerical models," *Railway Eng. Sci.*, vol. 30, no. 4, pp. 403–436, Dec. 2022.
[33] Y.-S. Zhang, S.-L. Huang, and W. Zhao, "Detection system about steel cracks based on electronic ultrasonic," *NDT*, vol. 31, no. 4, pp. 307–310, 2009.
[34] Y. Gharaibeh, R. Sanderson, P. Mudge, C. Ennaceur, and W. Balachandran, "Investigation of the behaviour of selected ultrasonic guided wave modes to inspect rails for long-range testing and monitoring," *Proc. Inst. Mech. Eng., F, J. Rail Rapid Transit*, vol. 225, no. 3, pp. 311–324, May 2011.

CONG JIN was born in Jilin, China, in 1993. He received the B.S. degree in measurement and control technology and instrumentation from Liaoning University of Petroleum and Chemical Technology, Liaoning, China, in 2016. He is currently pursuing the master's degree in mechanical engineering with Xinjiang University, Xinjiang, China. His recent research interests include the effects of structural defects on antenna wheel-rails and antenna performance, and the study of damage detection systems. He is also working on various non-destructive testing methods.

YOU BAN was born in Xiayi, Henan, China, in 1990. He received the B.S. degree in mechanical design, manufacturing, and automation and the Ph.D. degree in mechanoelectronic engineering from Xidian University, Xi'an, China, in 2013 and 2020, respectively. He joined the School of Intelligent Manufacturing Modern Industry (School of Mechanical Engineering), Xinjiang University, Ürümqi, as an Associate Professor, in July 2020. His recent research interests include influence analysis of structural imperfectness on antenna performances, compensation techniques, and beam-forming design of large reflector antennas. He is also working on multidisciplinary synthetic design and optimization of various antennas structure.

SHUFEI FENG was born in Henan, China, in 1993. He received the B.S. and Ph.D. degrees from Xidian University, Xi'an, China, in 2013 and 2019, respectively.

Since 2020, he has been a Lecturer with the School of Mechanical Engineering, Dongguan University of Technology, Dongguan, China. From September 2022 to September 2023, he was a Visiting Scholar with Katholieke Universiteit Leuven, Leuven, Belgium. His recent research interests include structural design and optimization of large reflector antennas.